

THE VARIABLE JET OF THE VELA PULSAR.

G. G. PAVLOV, M. A. TETER, O. KARGALTSEV, AND D. SANWAL

The Pennsylvania State University, 525 Davey Lab, University Park, PA 16802, USA

Submitted to *ApJ* 2002 November 27; accepted 2003 March 26; to be published 2003 July 10

ABSTRACT

Observations of the Vela pulsar-wind nebula (PWN) with the *Chandra X-ray Observatory* have revealed a complex, variable PWN structure, including inner and outer arcs, a jet in the direction of the pulsar's proper motion, and a counter-jet in the opposite direction, embedded in diffuse nebular emission. The jet consists of a bright, 8''-long inner jet, between the pulsar and the outer arc, and a dim, curved outer jet that extends up to $\sim 100''$ in approximately the same direction. From the analysis of thirteen *Chandra* observations spread over ≈ 2.5 years we found that this outer jet shows particularly strong variability, changing its shape and brightness. We observed bright blobs in the outer jet moving away from the pulsar with apparent speeds $(0.3\text{--}0.6)c$ and fading on time-scales of days to weeks. If the blobs are carried away by a flow along the jet, the observed variations suggest mildly relativistic flow velocities, about $(0.3\text{--}0.7)c$. The spectrum of the outer jet fits a power-law model with a photon index $\Gamma = 1.3 \pm 0.1$. For a distance of 300 pc, the apparent average luminosity of the outer jet in the 1–8 keV band is about 3×10^{30} erg s⁻¹, compared to 6×10^{32} from the whole PWN within 42'' from the pulsar. The X-ray emission of the outer jet can be interpreted as synchrotron radiation of ultrarelativistic electrons/positrons. This interpretation allows one to estimate the magnetic field, ~ 100 μ G, maximum energy of X-ray emitting electrons, $\sim 2 \times 10^{14}$ eV, and energy injection rate, $\sim 8 \times 10^{33}$ erg s⁻¹, for the outer jet. In the summed PWN image, we see a faint, strongly bent, extension of the outer jet. This bending could be caused by combined action of a wind within the supernova remnant, with a velocity of a few $\times 10$ km s⁻¹, along with the ram pressure due to the pulsar's proper motion. The more extreme bends closer to the pulsar, as well as the apparent side motions of the outer jet, can be associated with kink instabilities of a magnetically confined, pinched jet flow. Another feature found in the summed image is a dim, $\sim 2'$ -long outer counter-jet, which also shows a power-law spectrum with $\Gamma \approx 1.2\text{--}1.5$. Southwest of the jet/counter-jet (i.e., approximately perpendicular to the direction of pulsar's proper motion), an extended region of diffuse emission is seen. Relativistic particles responsible for this radiation are apparently supplied by the outer jet.

Subject headings: ISM: jets and outflows — pulsars: individual (Vela) — stars: neutron — stars: winds, outflows — supernova remnants: individual (Vela) — X-rays: stars

1. INTRODUCTION

Thanks to the outstanding angular resolution of the X-ray telescopes aboard the *Chandra X-ray Observatory*, we are able to study the structure of pulsar-wind nebulae (PWNe), formed by relativistic outflows from pulsar magnetospheres. Particularly detailed *Chandra* images have been obtained for PWNe around the Crab pulsar (Mori et al. 2002; Hester et al. 2002), Vela pulsar (Helfand, Gotthelf, & Halpern 2001; Pavlov et al. 2001a), and PSR B1509–58 (Gaensler et al. 2002). Each of these images shows an approximately axially-symmetric PWN morphology, with an extended structure stretched along the symmetry axis. This suggests that such structures, usually called *jets*, are common to at least young pulsars. Most likely, these jets are associated with collimated outflows of relativistic particles along the pulsar's rotation axes. Investigations of pulsar jets allow one to understand the origin and properties of pulsar winds and their interaction with the ambient medium. Moreover, since jets have been observed in many astrophysical objects (e.g., AGNs, Galactic microquasars), studying pulsar jets may shed light on the mechanism of jet formation in these objects as well.

Due to its proximity ($d \simeq 300$ pc, from the annual parallax of the Vela pulsar — Caraveo et al. 2001; Dodson et al. 2003a), the Vela PWN is particularly well suited for studying the pulsar outflows. This PWN was discovered with *Einstein* (Harnden et al. 1985) and studied extensively with *ROSAT*

and *ASCA* (Markwardt & Ögelman 1998, and references therein). The *Einstein* and *ROSAT* observations with the High Resolution Imagers (HRIs) have established the overall kidney-bean shape of the Vela PWN, with a symmetry axis approximately co-aligned with the pulsar's proper motion. The first observations of the Vela PWN with *Chandra* (Pavlov et al. 2000; Helfand et al. 2001) have shown a detailed structure of the nebula, including inner and outer arcs, northwest and southeast jets, and bright knots in the southeast part of the PWN. Furthermore, Pavlov et al. (2001a) found that the nebula elements were variable in position, brightness, and, perhaps, spectrum. Based on two observations with the *Chandra's* Advanced CCD Imaging Spectrometer (ACIS), Pavlov et al. (2001a) noticed a long, curved extension of the northwest jet in approximately the same direction, well beyond the apparent termination point of the bright “inner jet” at its intersection with the outer arc. This dim “outer jet” (dubbed “filament” in that paper) had a brighter “blob” close to the jet's end, which showed particularly strong displacement between the two observations taken 7 months apart.

To understand the nature of the variability of the Vela PWN, we carried out a series of eight monitoring observations with the *Chandra* ACIS. These observations have confirmed the dynamical structure of the PWN, with most dramatic changes occurring in the outer jet. Moreover, we were able to detect an “outer counter-jet”, a much dimmer extension of the southeast (counter-)jet, which is clearly seen only in the summed image, together with highly asymmetric diffuse emission. In

the present paper, we concentrate mainly on the highly variable outer jet, which has been detected in ten ACIS observations and three observations with the High Resolution Camera (HRC), deferring a detailed analysis of the other PWN elements to a future work.

We describe the observations, their analyses, and observational results in §2, and discuss possible interpretations in §3. The summary of our results and concluding remarks are presented in §4.

2. OBSERVATIONS AND DATA ANALYSIS

2.1. ACIS observations

Series of ten ACIS observations of the Vela pulsar and its PWN were carried out from 2000 April 30 through 2002 August 6. The dates of the observations and the exposure times are given in Table 1. In all observations the target was imaged on the back-illuminated chip S3, less affected by the radiation-induced changes in CCD charge transfer efficiency than the front-illuminated chips. To image the whole PWN on one chip, the pulsar was offset from the ACIS-S aim-point by $-1'.5$ along the chip row in each observation. In the first two observations only half of the chip was read out (1/2 Subarray mode), with a frame time of 1.5 s, to reduce the pile-up from the bright pulsar. The rest of the observations were done in the Full Array mode, with a frame time of 3.24 s. The telescope focal plane temperature for all ACIS observations was -120 C. We used the CIAO software¹, v.2.2.1 (CALDB 2.10) for the data analysis, proceeding from Level 1 event files. The energy and grade of each event were corrected for charge transfer inefficiency (CTI) using the tool developed by Townsley et al. (2000).

To examine the changes in the PWN surface brightness, we have scaled the number of counts per pixel for each of the ten ACIS observations as $N'_i = N_i(t_5/t_i)$, where t_i is the effective exposure time of i -th observation, and $t_5 = 17933$ s is the exposure time of the reference observation (ObsID 2813). In addition, we restricted the energy range to 1.0–8.0 keV to reduce the background contribution at higher energies and get rid of the trailed images (readout streaks) produced by the bright pulsar, whose spectrum is softer than that of the PWN. To produce adaptively smoothed images, we use the CIAO tool `csmooth`, with the smoothing scale such that the signal-to-noise ratio is between 4 and 5.

Applying the CIAO tool `wavdetect` to the individual images, we found 15 point-like sources on the S3 chip; 9 of them, including the Vela pulsar, we seen in at least 4 images. The rms deviation of the *Chandra* pipe-line coordinates of 8 of the 9 sources is $\leq 0''.7$, while for one off-axis source it is about $1''.4$. This source is likely extended because `wavdetect` finds two sources in some of the images. Therefore, we exclude this source and conclude that the astrometry is better than $0''.7$. We will use this value as the uncertainty of the coordinate measurements.

2.2. HRC observations

To increase the total time span and the sampling, we also included three archival *Chandra* HRC observations in our analysis (see Table 1 for the ObsIDs and exposure times). In all the three observations the Vela PWN was imaged on the HRC-I (imaging) plate. Pipe-line processed Level 2 event files from

the archive were used for the analysis, without further reduction. We scaled the binned images to the 2000 January 20 exposure time and adjusted the color scale to reveal the similar amount of detail that was seen in the ACIS images. To produce the smoothed images, each image was binned at a 2 pixel by 2 pixel scale and then smoothed similar to the ACIS images.

TABLE 1
SUMMARY OF THE OBSERVATIONS.

Panel	Obs ID	Instrument	Date of observation	Exposure time (s)
1	1518	HRC-I	2000-01-20	49,765
2	364	HRC-I	2000-02-21	48,050
3	128	ACIS-S	2000-04-30	10,577
4	1987	ACIS-S	2000-11-30	18,851
5	2813	ACIS-S	2001-11-25	17,933
6	2814	ACIS-S	2001-11-27	19,870
7	2815	ACIS-S	2001-12-04	26,960
8	2816	ACIS-S	2001-12-11	18,995
9	2817	ACIS-S	2001-12-29	18,938
10	1966	HRC-I	2002-01-13	49,464
11	2818	ACIS-S	2002-01-28	18,663
12	2819	ACIS-S	2002-04-03	19,920
13	2820	ACIS-S	2002-08-06	19,503

2.3. Spatial structure

The large-scale X-ray structure of the Vela PWN is shown in the summed ACIS image of observations 2813–2820 in Figure 1. The brightest, kidney-shaped part of the PWN (white and yellow in Fig. 1) is approximately symmetric with respect to the direction of the pulsar’s proper motion (PA $\simeq 307^\circ$, in the Local Standard of Rest — see Caraveo et al. 2001, and references therein). This deep image clearly reveals a long ($\approx 1'.7$, as measured from the pulsar) outer jet, approximately in the direction of the proper motion, which is somewhat curved and brightened at its end. A much fainter outer counter-jet is seen, for the first time, in the opposite direction. Finally, we see highly asymmetric diffuse emission feature southwest of the jet/counter-jet line, which is obviously connected to the “main body” of the PWN.

Choosing different brightness scale and color scheme, one can resolve a fine structure within the bright core of the PWN. It is depicted in Figure 2 which shows a zoomed individual image of 2002 January 28. The most apparent elements of this structure, with the pulsar [1] at the center, are the inner arc [2], the outer arc [3], the inner jet [4], and the inner counter-jet [5]. The inner jet is directed northwest from the pulsar (PA $\simeq 307^\circ$) in the direction of the pulsar’s proper motion, and the counter-jet is directed toward the southeast (PA $\simeq 127^\circ$ — Pavlov et al. 2000). The bright core (red and yellow in Fig. 2) is surrounded by a “shell” [6] of diffuse emission (green in Fig. 2). The outer jet [7] looks like an extension of the much brighter inner jet, well beyond the apparent termination point of the inner jet at its intersection with the outer arc. It is clearly seen on this image, contrary to the much dimmer outer counter-jet. Comparison of the individual images shows that all the PWN elements are variable, especially the outer jet. Throughout this paper, we will concentrate our analysis upon the dynamic outer jet, though the inner jet and counter-jet will be considered for comparison.

¹ Chandra Interactive Analysis of Observations — see <http://cxc.harvard.edu/ciao/>.



FIG. 1.— Merged smoothed image, $4'6 \times 3'6$, of the Vela PWN scaled to show the outer jet and outer counter-jet (northwest and southeast of the bright PWN core, respectively), and the faint diffuse emission southwest of the core. In all images in this paper North is up and East to the left.

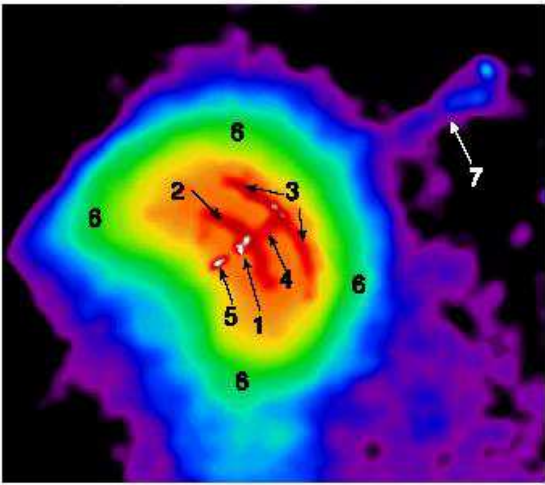


FIG. 2.— *Chandra* ACIS-S3 image, $2'1 \times 2'7$, of the Vela PWN showing the structural elements: (1) the Vela pulsar, (2) the inner arc, (3) the outer arc (4) the inner jet, (5) the counter jet, (6) the shell, (7) the outer jet.

The outer jet extends away $\approx 0.14d_{300}$ pc ($4.3 \times 10^{17}d_{300}$ cm = $0.45d_{300}$ lt-yr) from the pulsar, where d_{300} is the distance to the pulsar in units of 300 pc. The characteristic width (diameter) of the outer jet is about $3 \times 10^{16}d_{300}$ cm. Because the outer jet is generally co-aligned with the inner jet, it is natural to assume that the inner and outer jets are connected at the intersection with the outer arc, although the dim outer jet can hardly be seen within the shell. Figure 2 shows a typical view of the outer jet structure. It is not as straight as the inner jet; in this image it slightly bends southward from the inner jet/counter-jet direction, and back to the north near the end. Other individual images (Figs. 3 and 4) show different, sometimes more extreme, bending (e.g., panel 2 in Fig. 3 and panel 13 in Fig. 4).

The average (background-subtracted) surface brightness of the outer jet in the ten ACIS images is about 0.05 counts $\text{arcsec}^{-2} \text{ks}^{-1}$, in the 1–8 keV band, with extremes of variability from 0.032 ± 0.004 to 0.060 ± 0.003 , in the same units (errors here and below are 1σ errors). It is seen from Figures

1 and 2, that the outer jet brightness varies along its length. Choosing yet another brightness scale (Figs. 3 and 4), we resolve compact regions of enhanced emission within the outer jet (blobs, hereafter), with brightness up to 0.16 ± 0.02 counts $\text{arcsec}^{-2} \text{ks}^{-1}$, typically 2–3 times brighter than the remainder of the outer jet. In turn, the outer jet is approximately 3 times brighter than the background on the northeast side of the jet, with brightness 0.021 ± 0.002 counts $\text{arcsec}^{-2} \text{ks}^{-1}$. The background on the southwest side of the outer jet is about 50% brighter than that on the northeast side. This difference is quite clearly seen from Figure 1, which also shows that the increased background is connected to a region of enhanced diffuse emission on the southwest side of the bright PWN. The average surface brightnesses of the inner jet and counter-jet are 1.5 and 1.8 counts $\text{arcsec}^{-2} \text{ks}^{-1}$, respectively, ranging from 1.1 to 1.9 for the inner jet and from 1.3 to 2.8 for the counter-jet, with typical errors of 0.2 counts $\text{arcsec}^{-2} \text{ks}^{-1}$. The background-subtracted surface brightness of the outer counter-jet is ≈ 0.007 counts $\text{arcsec}^{-2} \text{ks}^{-1}$, as measured from the summed image in Figure 1.

2.4. Spatial variation

Figures 3 and 4 give the time sequence of the ACIS-S3 and HRC-I observations for the outer jet. Each of the panels corresponds to the appropriate data set from Table 1. The variability of the outer jet is clearly seen, in both the HRC and ACIS images. Over the thirteen observations, with different periods of time between each of them, we distinguish three different types of variability in the outer jet. First, the outer jet shifts from side to side, bending and apparently twisting. Second, the blobs move outward along the outer jet. Finally, the blobs change in brightness and eventually disappear.

A very vivid example of the structural change in just one month is demonstrated by the first two *Chandra* HRC observations (panels 1 and 2 of Fig. 3). In panel 1, the outer jet looks like a “hook” attached to the bright spot on the outer arc, with the outer end of the hook pointing due north and terminating at an elongated blob. In panel 2, the hook evolved into a much more bent loop-like structure, which terminates with apparently the same (albeit fainter) blob at approximately the same location. The structure has moved between two observations, indicating that the sideways shift (e.g., from point P in panel 1 to point Q of panel 2) is approximately $12''$ in the 32 days separating the observations. This translates to a sideways speed of $0.6 c$ (all the speeds in this section are given for $d = 300$ pc). Another example is presented by the first two ACIS images (panels 3 and 4) separated by 7 months. The shape of the outer jet has changed from pointing due north and terminating with a blob to an S-shaped structure. The displacement of the blob (which easily could be another blob given that the time between the observations is so long) suggests a speed $\gtrsim 0.1c$. In observations 5–11 (Fig. 4) the jet appears almost straight, with a slight southward curve. The short time (16 days) between the fifth and eighth observations suggests that the sideways shifts of the jet occur on a time scale of order of weeks. A dramatic change of the jet shape is again seen in the last observation 13, separated by 4 months from the previous observation. In the last image, the jet points due west beyond the PWN shell and then abruptly turns to the north, with a bright blob at the turning point. Overall, the small-scale structural changes are seen in all of the observations. For instance, the “base” of the outer jet (where it leaves the shell — see the white boxes in Figs. 3 and 4) shifts from one observation to the next. Figure 5 shows smoothed one-

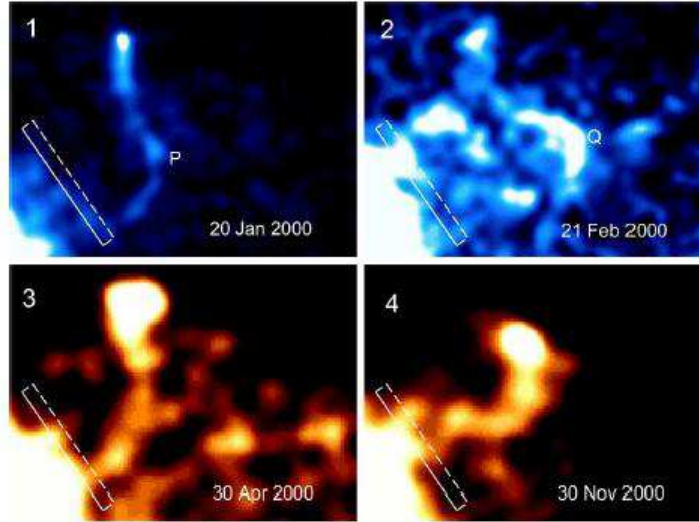


FIG. 3.— Images of the outer jet from the observations of year 2000. The HRC-I and ACIS-S3 images are in blue and orange, respectively. The panels are numbered in accordance with Table 1. The size of each panels is $73'' \times 53''$. The boxes, $28'' \times 2''6$, at same sky position in all the panels, are overplotted to guide the eye. The points P and Q mark westward extremes of the bent jet in the two HRC observations; they were used to estimate the jet's motion between the two observations (see text for details).

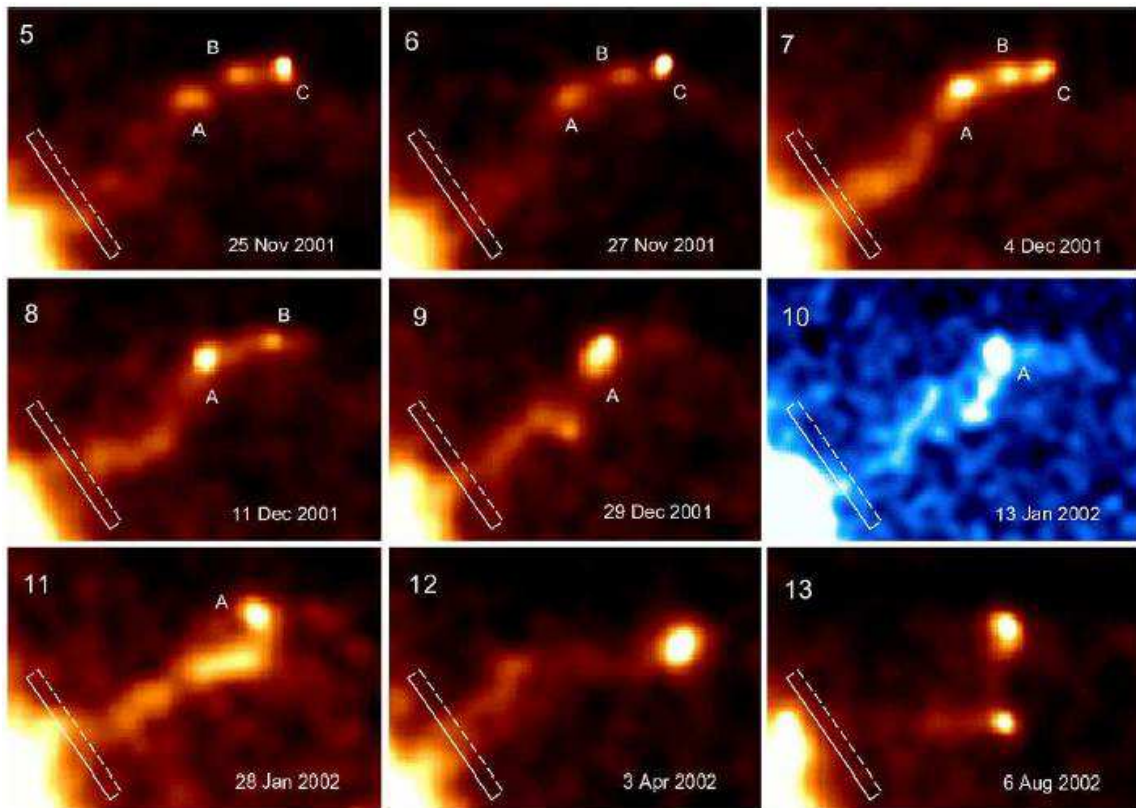


FIG. 4.— Sequence of *Chandra* images of the outer jet observed in 2001–2002. The $73''$ by $53''$ panels are numbered according to Table 1. The letters A, B, and C label the moving bright blobs identified in observations 5 through 11. The boxes, $28'' \times 2''6$, at same sky position in all the panels, were used to demonstrate the jet's sideways motions (see Fig. 5).

dimensional distributions of counts across the outer jet (i.e., along the length of the narrow boxes in Fig. 4) in eight consecutive ACIS observations. Typical apparent speeds of these shifts are of order a few tenths of speed of light.

The apparent speeds of the blobs along the jet are of similar magnitude. The proper motions of the blobs A and B seen in several panels of Figure 4 are shown in Figures 6 and 7. The $1''$ uncertainty of the position of the blobs is obtained by adding in quadrature the $0.7''$ uncertainty from the astrometry and an additional uncertainty, of approximately the same value, from measuring the centroid of the blob from the smoothed images. Blob B vanishes in panel 9, so its apparent speed is calculated from four observations. The apparent speeds of blobs A and B are $(0.35 \pm 0.06)c$ and $(0.51 \pm 0.16)c$, respectively. Blob C vanished quickly, having an (unconstrained) apparent speed of $(0.6 \pm 0.7)c$. Assuming that the measurements of the apparent velocities of the blobs inside the outer jet give the bulk flow speed, $v_{\text{flow}} \sim (0.3-0.7)c$, and the jet does not deviate strongly from the sky plane, we obtain $t_{\text{flow}} = l_{\text{jet}}/v_{\text{flow}} \sim (0.6-1.5)$ yr for the travel time along the jet. The actual travel time may be significantly different if the jet direction strongly deviates from the sky plane and relativistic effects are important (see §3.1).

The blobs change brightness as they move and disappear. For instance, blob C slightly brightens in two days between observations 5 and 6, then fades somewhat between observations 6 and 7, and disappears completely after another week (by observation 8). Similarly, the brightness of blob B changes noticeably through observations 5–8, while this blob vanishes in observation 9. No such blobs are found in either the inner jet or the counter-jet.

2.5. Spectrum and luminosity

For the spectral analysis of the jets in the ACIS data, we used the XSPEC package, v.11.2.01. In all spectral fits we used the hydrogen column density fixed at $n_{\text{H}} = 3.2 \times 10^{20}$ cm^{-2} , as determined from the observation of the Vela pulsar with the *Chandra* Low-Energy Transmission Grating Spectrometer (Pavlov et al. 2001b). Furthermore, because of a build up of a contaminant on either the ACIS CCDs or the filters, additional time-dependent absorption is accounted for in the spectral fits using the ACIS_ABS model (see Plucinsky et al. 2002). The degree of absorption was set by the number of days since *Chandra* launch. Only photons in the energy range of 1–8 keV were used for fitting to avoid contaminations from readout strips from the piled-up pulsar and to reduce the charged particle background.

The photons from the outer jet were extracted using polygons (of somewhat different areas for the different observations — see Table 2) which enclosed the entire structures beyond the PWN shell. Two background regions were chosen — the first from a dark region north of the outer jet (background A), and the second sandwiching the outer jet (background B). Various spectral models for emission from an optically thin thermal plasma were attempted to test if the emission associated with the outer jet is due to an interaction of the jet with the ambient (SNR) gas. The overall fits are formally acceptable, but the corresponding plasma temperatures, about 30 keV, are very high, in accordance with the lack of spectral lines in the spectra. At such high temperatures these models are equivalent to the thermal bremsstrahlung model, which, with the statistics available, is indistinguishable from a power-law at energies of interest. The power-law model, $f(E) = N_{\Gamma}(E/1 \text{ keV})^{-\Gamma}$, is more physical than

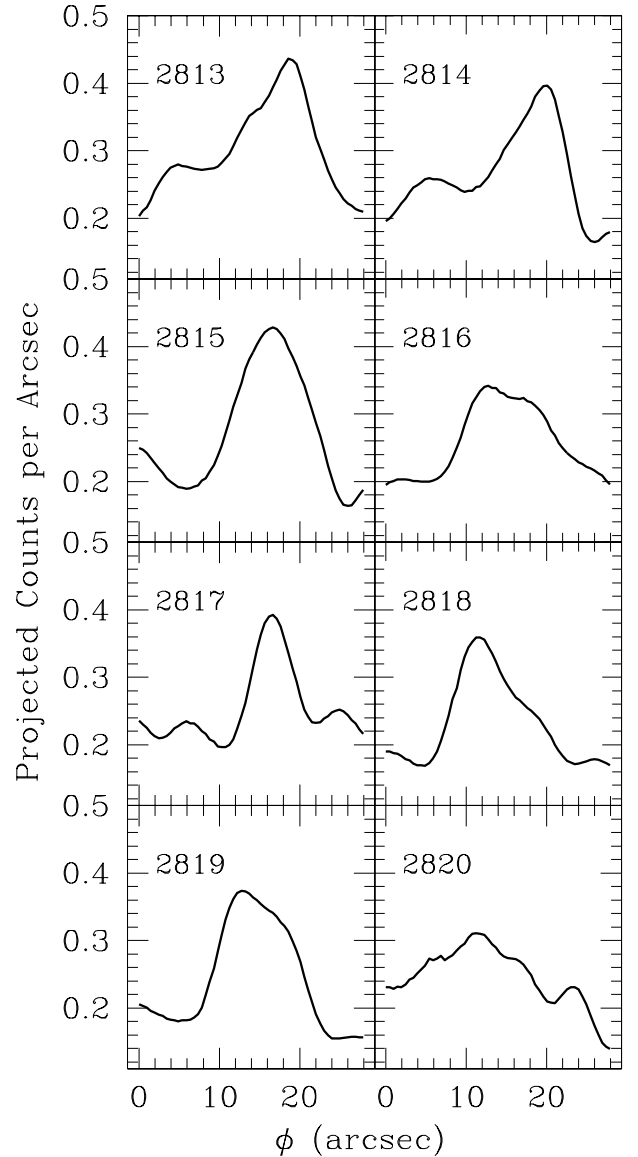


FIG. 5.— Smoothed distributions of counts across the outer jet at a distance of $50''$ from the pulsar in eight ACIS observations (ObsID 2813–2820). The number of counts (per arcsecond) integrated along the short dimension of the boxes in Figure 4 is plotted as a function of coordinate ϕ along the box length.

the high-temperature bremsstrahlung because it naturally describes non-thermal (e.g., synchrotron) radiation; therefore, we use it for the spectral analysis of the jets.

An example of the power-law fit to a data set combined of observations 2813–2816, chosen because of the similar extraction areas and locations on the chip, is shown in Figure 8, for background B. The results of the fits of the outer jet spectra with the power-law model for each of the individual ACIS observations are given in Table 2, for both backgrounds A and B. Figure 9 shows the contours of the photon index Γ versus spectral brightness at 1 keV, $\mathcal{B} = N_{\Gamma}/A$ (where A is the area of the extraction region — see Table 2). For each of the two backgrounds, the variability of the photon index is statistically insignificant, contrary to the variability of the brightness. Joint spectral fits (fitting all data simultaneously with a common index and individual normalizations)

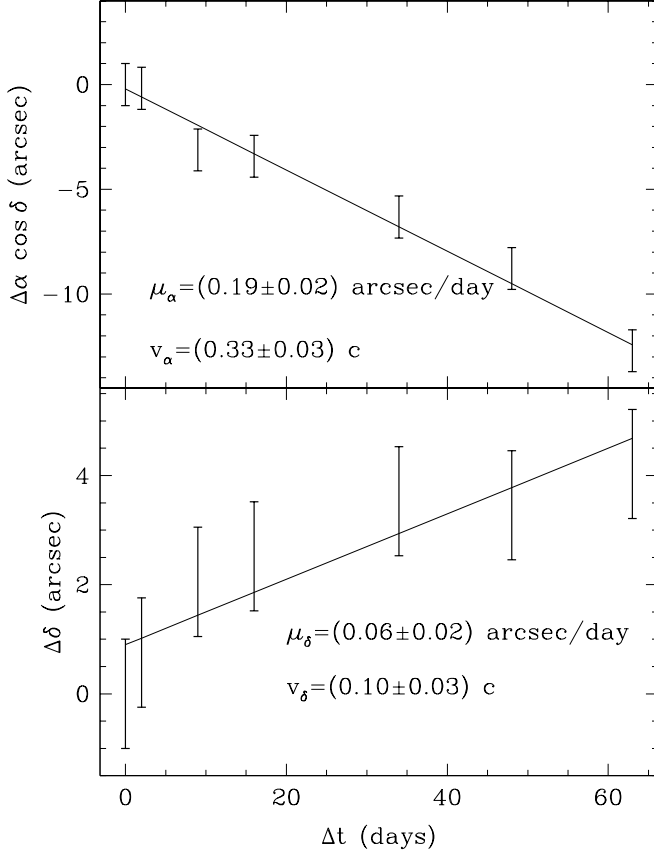


FIG. 6.— Proper motion of blob A in panels 5–11 of Figure 4. The upper and lower panels show the motions along the right ascension and declination, respectively. The straight lines are the least-square fits assuming constant speeds. Under this assumption, the apparent speed of blob A is $(0.35 \pm 0.06)d_{300}c$.

give $\Gamma = 1.36 \pm 0.04$ and 1.27 ± 0.04 for backgrounds A and B, respectively, coinciding with the weighted average indices that are calculated from the individual fits for each of the two backgrounds. The difference between the average indices can be ascribed to systematic effects associated with the choice of background. Since it is not immediately clear which of the two backgrounds is more adequate, we adopt a conservative estimate, $\Gamma = 1.3 \pm 0.1$, consistent with both background choices.

We searched for a change in power-law index along the length of the outer jet by extracting regions near the beginning of the outer jet, where it exits the shell of the bright PWN, and at its end. Because of the low number of counts, a joint fit of all the ACIS observations was attempted. The normalizations for each observation were allowed to vary (because the extraction areas were different), while the photon index for all observations was fit to a common value. The fits to these combined spectra were statistically acceptable, with $\chi^2_{\nu} = 1.19$ (82 degrees of freedom [dof]) and $\chi^2_{\nu} = 0.97$ (96 dof) for the beginning and the end of the outer jet, respectively (using background B). The change of the index, from 1.36 ± 0.09 at the jet beginning to 1.25 ± 0.08 near its end, is not statistically significant.

We also attempted to compare the spectra of the blobs with each other and with the spectrum of the rest of the outer jet. For individual observations, no differences are seen because

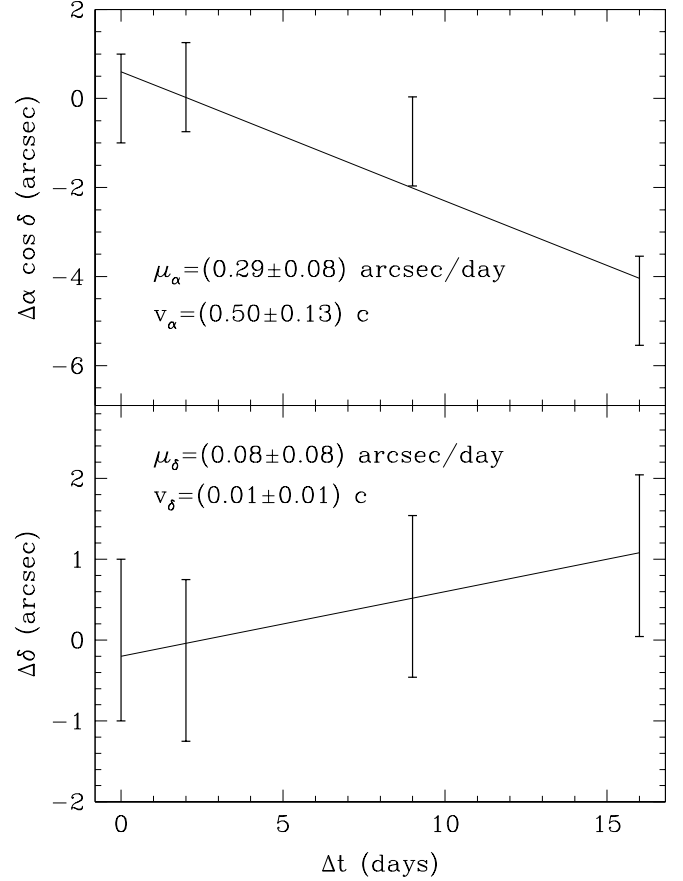


FIG. 7.— Proper motion of blob B in panels 5–8 of Figure 4. The apparent speed of blob B is $(0.51 \pm 0.16)d_{300}c$.

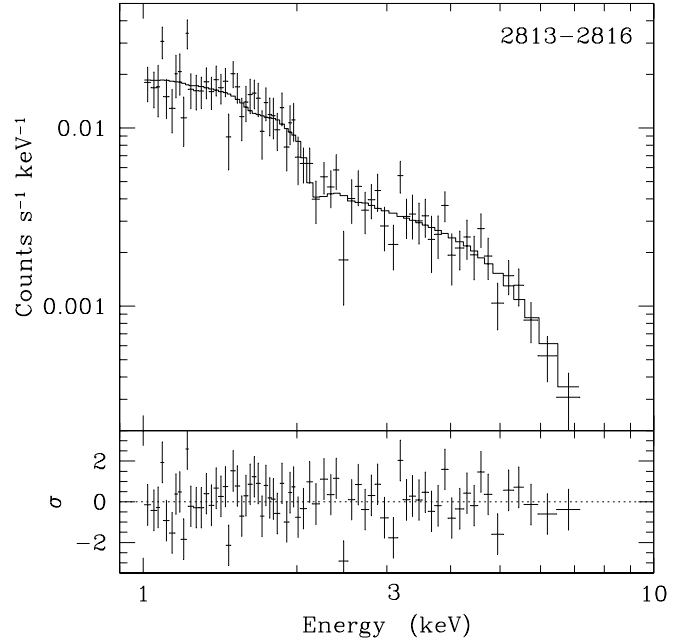


FIG. 8.— Power-law fit to the spectrum of the outer jet for the merged data set (observations 2813–2816). The best-fit parameters are $\Gamma = 1.29 \pm 0.06$, and $N_{\Gamma} = 3.90 \pm 0.40 \times 10^{-5}$ photons $\text{cm}^{-2} \text{s}^{-1} \text{keV}^{-1}$ at 1 keV ($\chi^2_{\nu} = 0.98$, for 68 dof).

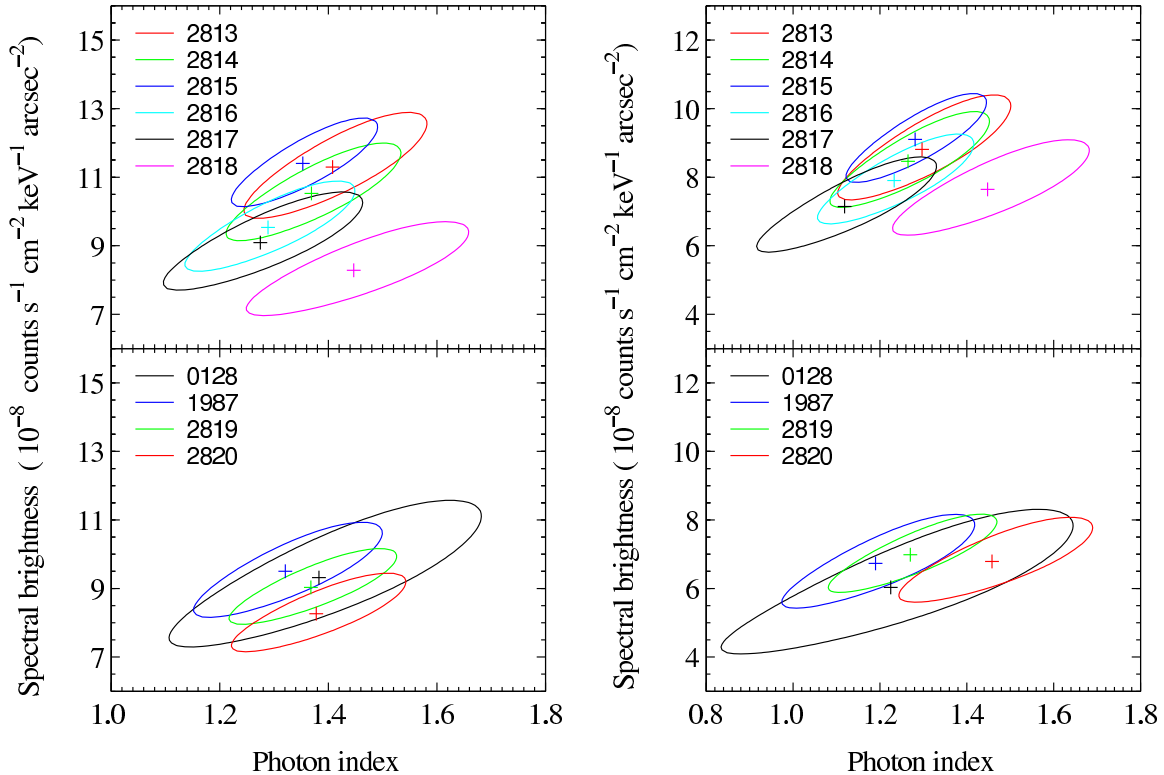


FIG. 9.— One-sigma confidence contours for photon index Γ and spectral surface brightness at 1 keV, $\mathcal{B} = N_{\Gamma}/A$, for 10 ACIS observations of the outer jet using background A (left panels) and background B (right panels). The contours are separated into the upper and lower panels for clarity of presentation.

TABLE 2
SPECTRAL PARAMETERS AND SURFACE BRIGHTNESSES FOR THE ACIS OBSERVATIONS OF THE OUTER JET.

ObsID	Area	Background A					Background B				
		Γ	N_{Γ}	S_B	χ^2_{ν}	dof	Γ	N_{Γ}	S_B	χ^2_{ν}	dof
0128	500	1.38 ± 0.20	4.7 ± 0.7	4.4 ± 0.4	0.71	13	1.23 ± 0.27	3.0 ± 0.7	3.2 ± 0.4	0.62	13
1987	400	1.32 ± 0.12	3.8 ± 0.4	5.7 ± 0.3	1.38	26	1.19 ± 0.15	2.7 ± 0.4	5.1 ± 0.4	1.44	26
2813	449	1.41 ± 0.11	5.1 ± 0.5	6.7 ± 0.3	0.91	28	1.30 ± 0.13	4.0 ± 0.5	5.6 ± 0.3	1.01	28
2814	449	1.37 ± 0.11	4.7 ± 0.4	7.0 ± 0.3	0.79	31	1.27 ± 0.13	3.8 ± 0.4	5.6 ± 0.3	0.81	31
2815	413	1.35 ± 0.09	4.7 ± 0.3	6.5 ± 0.3	0.82	41	1.28 ± 0.10	3.8 ± 0.4	6.0 ± 0.3	0.87	41
2816	455	1.29 ± 0.10	4.3 ± 0.4	7.3 ± 0.4	0.94	30	1.23 ± 0.11	3.6 ± 0.4	5.5 ± 0.4	1.02	30
2817	393	1.28 ± 0.13	3.6 ± 0.4	5.0 ± 0.3	1.02	27	1.12 ± 0.14	2.8 ± 0.4	5.5 ± 0.3	1.04	27
2818	480	1.45 ± 0.13	4.0 ± 0.4	3.6 ± 0.3	1.01	26	1.45 ± 0.15	3.7 ± 0.4	4.5 ± 0.3	1.02	26
2819	656	1.37 ± 0.10	5.9 ± 0.5	4.7 ± 0.2	0.87	38	1.27 ± 0.13	4.6 ± 0.5	4.5 ± 0.3	0.85	38
2820	614	1.38 ± 0.10	5.1 ± 0.5	5.0 ± 0.3	0.92	27	1.46 ± 0.15	4.1 ± 0.5	3.9 ± 0.3	1.05	27

Area is the polygon extraction area of the outer jet in arcsec². Normalization of the power-law spectrum, N_{Γ} , is in units of 10^{-5} photons cm⁻² s⁻¹ keV⁻¹ at 1 keV. Mean surface brightness, S_B , is in units of 10^{-2} counts arcsec⁻² ks⁻¹, in the 1–8 keV range.

of the low number of counts. Combined fits, using background B, yield the photon indices 1.36 ± 0.12 ($\chi^2_{\nu}=1.01$, 70 dof) for blob A (observations 2813–2818), 1.07 ± 0.19 ($\chi^2_{\nu}=0.47$, 20 dof) for blob B (observations 2813–2816), and 1.43 ± 0.21 ($\chi^2_{\nu}=1.27$, 18 dof) for blob C (observations 2813–2815). Thus, the spectral slopes do not show statistically significant differences even for the combined fits.

For the inner jet and inner counter-jet, we extracted the source counts from stretched elliptical areas of 12.7 and 18.5 arcsec², respectively, which enclose as much of the jet/counter-jet emission as possible without contamination from the other structures within the PWN, such as the arcs.

Because of the very nonuniform distribution of surface brightness around the inner jet and counter-jet, we had to take backgrounds from small regions; we chose circles (6.8 and 10.6 arcsec² for the inner jet and inner counter-jet, respectively) in the immediate vicinities northeast and southwest of the source extraction regions. The average values of the photon index for the inner jet and inner counter-jet, $\Gamma = 1.09$ and 1.20, respectively, appear somewhat smaller than that for the outer jet. However, the photon indices measured in individual observations show large deviations from the average values (rms deviations are 0.24 and 0.10, respectively), likely associated with statistical fluctuations of the bright background

estimated from small regions. Therefore, we cannot firmly establish the spectral differences between the outer jet and its inner counterparts from the data available.

As the outer counter-jet is hardly seen in the individual images, its spectrum was measured in the joint fit using observations 2813–2820. The source counts were extracted from a polygon area of 336 arcsec². Because of the faintness of the outer counter-jet, the fit is rather sensitive to the choice of background. Taking background from a region northeast of the end of the outer counter-jet, we obtain the photon index $\Gamma \approx 1.5$, while the index is smaller, $\Gamma \approx 1.2$, for the background from a region which sandwiches the outer counter-jet. Thus, the spectrum of the outer counter-jet remains poorly constrained, its slope being indistinguishable from that of the outer jet, within the uncertainties.

Assuming isotropic radiation, the average (unabsorbed) luminosities of the inner jet, inner counter-jet, and outer counter-jet, in the 1–8 keV band, are 2.6, 4.5 and 0.5×10^{30} erg s⁻¹, respectively, for $d = 300$ pc. The average luminosities are computed from the average spectral parameters of the various components. The outer jet demonstrates some variability in luminosity. For background A, the extremes of the luminosity are 2.7 ± 0.3 and $4.4 \pm 0.4 \times 10^{30}$ erg s⁻¹, with an average of 3.4×10^{30} erg s⁻¹. For background B, the outer jet luminosity varies from 2.4 ± 0.3 to $3.8 \pm 0.4 \times 10^{30}$ erg s⁻¹, with an average of 3.0×10^{30} erg s⁻¹. For comparison, the luminosity of the whole PWN within 42'' of the pulsar is $L_{\text{pwn}} = 6.0 \times 10^{32}$ erg s⁻¹, in the same energy band.

3. DISCUSSION.

The detected variability of the outer jet is the most vivid demonstration of the dynamical behavior of the Vela PWN. The observed changes of the overall shape of the outer jet over a time scale of weeks suggest apparent speeds up to $(0.3\text{--}0.7)d_{300}c$, which is comparable to the apparent speeds of the blobs moving along the outer jet away from the pulsar. The spectra of the outer jet, as well as those of the other PWN elements, fit well with a power-law model, indicating that this is radiation from ultrarelativistic particles. These observations allow one to assume that the outer jet is associated with a polar outflow of relativistic particles from the pulsar's magnetosphere². Possible implications of our observational results are discussed below.

3.1. Geometry

The orientation of the jets is the most important item for explaining the observed dynamical behavior, evaluating the velocities, and calculating the energetics of these outflows. Immediately after the first *Chandra* observations of the Vela PWN, it was suggested that the bright (inner) jet and counter-jet are co-aligned with the rotational axis of the pulsar and, presumably, with the direction of pulsar's velocity (Pavlov et al. 2000; Helfand et al. 2001). As we have seen from Figures 3 and 4, the projection of the outer jet on the sky plane may strongly deviate from the (straight) extension of the projection of the inner jet/counter-jet. However, the outer jet projection was close to that line during the period of 2001 November 25 through 2002 January 13, when the apparent velocities of the bright blobs were measured. Assuming, by analogy with

the jets in AGNs and Galactic microquasars, that the apparent motion of blobs is associated with motion of matter along an approximately straight line (e.g., the three-dimensional velocities of the blobs coincide with the bulk flow velocity), one can constrain the true speed, $v = \beta c$, and the angle θ between the line of sight and the direction of motion. The apparent speed, $v_a = \beta_a c$, is related to the true speed by the equation $\beta_a = \beta \sin \theta (1 - \beta \cos \theta)^{-1}$. Figure 10 shows the dependence $\beta(\theta)$ for typical β_a inferred from the observed motions of the blobs. For $0.3 < \beta_a < 0.7$, the blobs can be approaching ($\theta < 90^\circ$) as well as receding ($\theta > 90^\circ$). The range of minimum values of β is $0.28 < \beta_{\text{min}} < 0.57$ (at $73^\circ > \theta > 55^\circ$), while the range of maximum allowed θ (at which $\beta \rightarrow 1$), is $147^\circ > \theta_{\text{max}} > 110^\circ$. The latter values are smaller than the $\theta = 155^\circ$, inferred by Helfand et al. (2001) under the assumption that the PWN arcs are Doppler-brightened parts of a torus around the jet/counter-jet, and they are smaller than the $\theta = 152^\circ$ suggested by Pavlov (2000)³ assuming the arcs are Doppler-brightened parts of ring-like shocks in relativistic conical outflows. If we adopt, e.g., $\theta = 155^\circ$, then the maximum possible apparent speed (at $\beta \rightarrow 1$) is $0.22c$, which is below the lower limits of $0.30c$ and $0.38c$ on the apparent speeds of blobs A and B at $d = 300$ pc. Thus, if any of the above-mentioned interpretations of the arcs and the inner jet/counter-jet are correct, we have to conclude that the outer jet is tilted from the pulsar rotation axis towards the observer even if its projection onto the sky looks almost straight, like in panels 5–9 of Figure 4. Moreover, we cannot rule out the possibility that the outer jet in these observations is strongly bent in the plane perpendicular to the sky plane — e.g., similar to the jet's sky projections in panels 1, 2 or 13. In this case the directions of the local flow velocities vary along the jet, which might explain the different apparent velocities of the blobs A and B. Such bending opens up a possibility that the bright regions of the jet are merely due to the projection effect — the segments of a uniformly bright, bent jet, which are oriented along the line of sight, appear brighter because of the increased optical depth, and the brightness is further enhanced by the Doppler boosting if the flow in these segments is streaming toward the observer. For instance, if the loop-like jet in panel 2 of Figure 3 were a two-dimensional structure, the southern segment of the loop would look like a bright blob if it were observed from the southwest direction. If this interpretation is correct, then the observed motions are caused by changing geometrical shape of the jet rather than the flow of locally bright material along the jet. An argument against such an interpretation is that the outer jet apparently terminates with a bright blob in at least 10 of 13 observations, and it is hard to believe that the end segment of a randomly bent jet is so often directed toward the observer. However, the extension of the jet beyond these bright blobs, as seen in the summed image of Figure 1 (see also §3.3), suggests that this may still be the case.

Another interesting fact related to the jet geometry is that the outer jet is consistently brighter than the outer counter-jet, with the ratio of surface brightnesses $f_b = 4\text{--}9$ (the large uncertainty in the brightness ratio is due to the nonuniform backgrounds). If the two jets are energetically similar and, on average, are oriented along a straight line, then the outer jet is approaching while the outer counter-jet is receding, contrary to the receding inner jet and approaching inner counter-jet in the geometry assumed by Pavlov et al. (2000) and Helfand

² An alternative interpretation — that the “outer jet” is a limb-brightened shell (northeast boundary) of a large diffuse nebula southwest of the pulsar (see Fig. 1) or a shock front — looks very unlikely, given the observed variations of its shape and, particularly, the moving blobs.

³ see also http://online.itp.ucsb.edu/online/neustars_c00/pavlov/oh/34.html

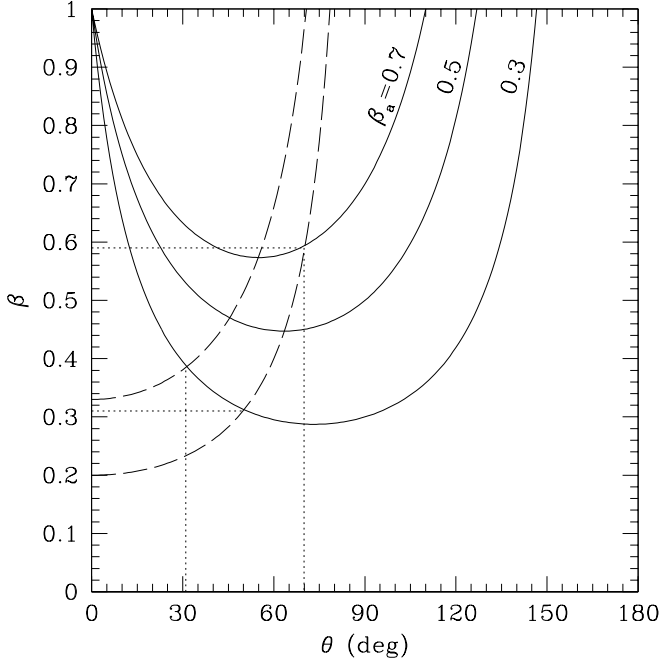


FIG. 10.— True speed $\beta = v/c$ versus angle θ between the line of sight and direction of motion for three values of the apparent speed $\beta_a = v_a/c$. The dashed lines ($\beta \cos \theta = 0.20$ and 0.33) bracket the domain of allowed β, θ assuming intrinsically similar outer jet and outer counter-jet streaming in opposite directions. See text for details.

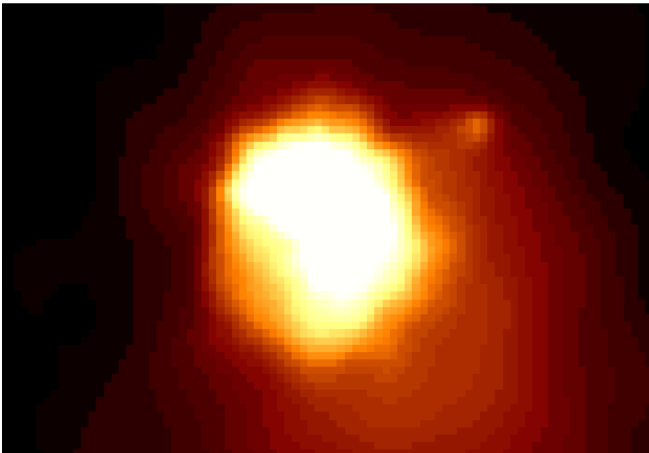


FIG. 11.— Smoothed ROSAT HRI image ($5'7 \times 3'8$) of the Vela PWN from the observation of November of 1997 (exposure 33 ks). The blob to the northwest of the PWN is indication that the outer jet has persisted at least 5 years.

et al. (2001). Within this interpretation, the brightness ratio is $f_b = [(1 + \beta \cos \theta)/(1 - \beta \cos \theta)]^{\Gamma+2}$, where Γ is the photon index. For $f_b = 4-9$ and $\Gamma = 1.2-1.4$, it gives $\beta \cos \theta = 0.20-0.33$, $\theta < 71^\circ-78^\circ$. Furthermore, these values of $\beta \cos \theta$ are consistent with $\beta_a = 0.3-0.7$, inferred from the blob's motion, if $0.31 < \beta < 0.59$ and $31^\circ < \theta < 70^\circ$ (see Fig. 10). To reconcile this result with the previously suggested orientation of the inner jets, one has to assume that the outer jet is tilted by a large angle ($\approx 90^\circ-100^\circ$) from the inner jet direction towards the observer, while the outer counter-jet is tilted by a similar angle away from the observer. Contrary to the observed

variable bendings of the outer jet, such tilts would have persisted for at least 5 years, since we confirm the existence of the brighter outer jet as far back as the 1997 ROSATHRI observation (Fig. 11). It is not clear what could cause such persistent tilts. Furthermore, it is not clear why the outer jet and counter-jet are so much dimmer than their inner counterparts, and what causes the abrupt decrease of brightness in the outer jet and counter-jet, with bright knots at the junctions of the inner and outer parts. In particular, the transition from the inner jet to the outer jet apparently occurs at the intersection of the jet with the outer arc, which hints that the outer arc is not a part of a ring-like structure but an umbrella-like shell pierced by the jet (Kargaltsev et al. 2002). Such a shell could be a bow shock created by the (inner) jet in the ambient medium, or it could form as a result of compression of the plasma outflow (hence, amplification of the frozen-in magnetic field) by the pulsar's motion in the ambient SNR matter (similar to that suggested by Aschenbach & Brinkmann 1975 for the Crab PWN). Another possible effect of the pulsar's motion is distortion of the ring-like structure(s) (e.g., the post-shock region presumably associated with the inner arc) by the ram pressure of the ambient matter, if the pulsar's rotational axis is not co-aligned with its velocity. In this case the leading part of the ring can be flattened by the ram pressure so that the assumption that the ring's sky projection is a perfect ellipse can result in wrong values for the inclination angles. Finally, one could consider a possibility that the structures appearing as the bright inner jet and counter-jet are, in fact, merely traces of particle beams in conical outflows brightened by the Doppler boosting (e.g., Radhakrishnan & Deshpande 2001; Pavlov 2000), while the outer jet and counter-jet are the “true pulsar jets”. Such an assumption implies a quite different interpretation of the whole PWN. We will discuss these and other possible PWN models in a future paper. Currently, we cannot unambiguously determine the orientation of the jets or the true velocities. However, from the observed variations of the shape of the outer jet, with mildly relativistic apparent velocities, we can conclude that the true velocities are neither ultrarelativistic nor nonrelativistic; $0.3c$ and $0.7c$ can be adopted as conservative lower and upper limits.

3.2. Magnetic field and energetics

The power-law spectra of the outer jet and the other PWN elements can be interpreted as optically thin synchrotron emission from ultrarelativistic electrons (and/or positrons) with a power-law spectrum: $dN(\gamma) = K\gamma^{-p}d\gamma$, where $\gamma = \varepsilon/m_e c^2$ is the Lorentz factor, $\gamma_m < \gamma < \gamma_M$. The electron index p is related to the photon index as $p = 2\Gamma - 1$, i.e., $p = 1.4-1.8$ for $\Gamma \approx 1.2-1.4$ observed in the outer jet. A characteristic energy E of the synchrotron photon depends on γ and magnetic field B as $E \sim 5B_{-4}\gamma_8^2$ keV, where $B_{-4} = B/(10^{-4} \text{ G})$, $\gamma_8 = \gamma/10^8$. If the minimum and maximum energies of the photon power-law spectrum are E_m and E_M , respectively, then the corresponding boundaries of the electron power-law spectrum are $\gamma_m \approx 2.4 \times 10^7 [E_m/(y_{m,p}\delta)]^{1/2} B_{-4}^{-1/2}$ and $\gamma_M \approx 2.4 \times 10^7 [(E_M/(y_{M,p}\delta))]^{1/2} B_{-4}^{-1/2}$, where the photon energies are in units of keV, $\delta = (1 - \beta^2)^{1/2}(1 - \beta \cos \theta)^{-1}$ is the Doppler factor (βc is the speed of the bulk motion), and $y_{m,p}$ and $y_{M,p}$ are dimensionless factors. The values of these factors are given in Table II of Ginzburg & Syrovatskii (1965; GS65 hereafter); e.g., $y_{m,p} = 1.3$ and 1.8 , $y_{M,p} = 0.011$ and 0.032 , for $p = 1.5$ and 2.0 , respectively. We will use the well-known formulae for synchrotron radiation to estimate the magnetic

field and energetics of the outer jet. Since the bulk motions observed in the jet are only mildly relativistic ($\beta \sim 0.5$ is a plausible estimate), the Doppler factor is not strongly different from unity; moreover, its actual value is unknown because of the uncertain orientation of the jet. Therefore, we will neglect the bulk motion of the jet's matter for most of the estimates below.

From the *Chandra* ACIS observations, the power-law spectrum of the outer jet is seen in the energy range between $E_1 \approx 0.5$ keV and $E_2 \approx 8$ keV. Since $E_m < E_1$ and $E_M > E_2$, we can constrain the minimum and maximum energies of the electron power-law distribution: $\gamma_m < 1.4 \times 10^7 B_{-4}^{-1/2}$, $\gamma_M > 5 \times 10^8 B_{-4}^{-1/2}$.

One can put a lower limit on the magnetic field in the outer jet using the condition that the Larmor radius of most energetic electrons responsible for the X-ray emission, $r_L = 1.7 \times 10^{15} \gamma_8 B_{-4}^{-1} \text{ cm} \gtrsim 6 \times 10^{15} (E_2/8 \text{ keV})^{1/2} B_{-4}^{-3/2} \text{ cm}$, does not exceed the jet radius, $r_{\text{jet}} \approx 1.5 \times 10^{16} d_{300} \text{ cm}$. This condition gives $B \gtrsim 60 (E_2/8 \text{ keV})^{1/3} d_{300}^{-2/3} \mu\text{G}$.

An upper limit on the magnetic field can be estimated from the fact that the spectrum of the outer jet maintains its power-law shape (shows no appreciable spectral break) at the observed energies $E \lesssim 8$ keV up to the end of the outer jet. This means that the time of synchrotron losses, $t_{\text{syn}} = 5.1 \times 10^8 \gamma_8^{-1} B_{-4}^{-2} \text{ s}$, for the most energetic particles responsible for the observed X-ray spectrum [$\gamma_8 \gtrsim 4 B_{-4}^{-1/2} (E_2/8 \text{ keV})^{1/2}$] is longer (or comparable to) the flow time, $t_{\text{flow}} = l_{\text{jet}}/v_{\text{flow}} \approx 6.7 \times 10^7 l_{\text{jet},18} (\beta/0.5)^{-1} \text{ s}$, where $l_{\text{jet}} = 10^{18} l_{\text{jet},18} \text{ cm}$. This gives $B \lesssim 150 (E_2/8 \text{ keV})^{-1/3} (\beta/0.5)^{2/3} l_{\text{jet},18}^{-2/3} \mu\text{G}$, i.e., $B \lesssim 100\text{--}300 \mu\text{G}$ for plausible values of l_{jet} and β .

An independent estimate on the plasma parameters of the outer jet can be obtained from the brightness of the synchrotron radiation, assuming some value for the ratio $k_m = w_{\text{mag}}/w_{\text{rel}}$ of the magnetic energy density, $w_{\text{mag}} = B^2/(8\pi)$, to the energy density of relativistic particles, w_{rel} . We cannot exclude the possibility that there are some relativistic ions in the jet, in addition to the synchrotron-emitting electrons (e.g., Gallant & Arons 1994), so that $w_{\text{rel}} = (1+k_i)w_e$, where k_i is the ratio of the energy density of ions to the energy density of electrons, w_e . Making use of the standard formulae for synchrotron radiation (e.g., GS65; Pacholczyk 1970), one can express the magnetic field in terms of the observable parameters. For a tangled magnetic field (randomly distributed along the line of sight), we obtain

$$B = 27 \left\{ \frac{k_m(1+k_i)}{a_p(3-2\Gamma)} \left[E_{M,p}^{(3-2\Gamma)/2} - E_{m,p}^{(3-2\Gamma)/2} \right] \frac{\mathcal{B}_{-7}}{\bar{s}_{16}} \right\}^{2/7} \mu\text{G}, \quad (1)$$

where $\mathcal{B} = N_\Gamma/A = 10^{-7} \mathcal{B}_{-7}$ photons $(\text{cm}^2 \text{ keV arcsec}^2)^{-1}$ is the average spectral surface brightness at $E = 1$ keV, N_Γ is the normalization of the photon spectral flux measured in area A , $\bar{s} = 10^{16} \bar{s}_{16} \text{ cm}$ is an average length of the radiating region along the line of sight, $E_{m,p} = E_m/\gamma_{m,p}$, $E_{M,p} = E_M/\gamma_{M,p}$, E_m and E_M are the lower and upper energies of the photon power-law spectrum (in keV), and a_p is a numerical coefficient given by eq. (3.32) and Table II of GS65 (e.g., $a_p = 0.165$ and 0.117 for $p = 1.4$ and 1.8 [$\Gamma = 1.2$ and 1.4], respectively). The value of B depends on several unknown parameters. Particularly uncertain are the boundary energies of the photon power-law spectrum because of the lack of high-resolution observations outside the X-ray range. Fortunately, the dependence on these

energies is rather weak: $B \propto E_M^{(3-2\Gamma)/7}$ for $E_{m,p}^{1.5-\Gamma} \ll E_{M,p}^{1.5-\Gamma}$ (which implies $\Gamma < 1.5$), and $B \propto [\ln(56E_M/E_m)]^{2/7}$, for $\Gamma \simeq 1.5$. For $\mathcal{B}_{-7} \simeq 1$ (a typical spectral surface brightness at 1 keV — see Fig. 9), $\bar{s}_{16} \approx 2\text{--}10$ (the main reason of the uncertainty is the unknown spatial structure and orientation of the jet), and $\Gamma = 1.2\text{--}1.4$, we obtain $30 \mu\text{G} \lesssim B[k_m(1+k_i)]^{-2/7} \lesssim 200 \mu\text{G}$, for plausible ranges of E_M and E_m . It is usually assumed that $k_m \approx 1$ (equipartition condition), while the value of k_i is rather uncertain. For the lower limit on the equipartition field not to exceed the upper limit estimated from (the lack of) synchrotron cooling, k_i should not exceed $\sim 10^3$. Thus, given the uncertainty of the parameters, we can only state that the equipartition field is consistent with the above-estimated limits, and that a plausible estimate for a typical field in the jet is $B \sim 100 \mu\text{G}$, with an uncertainty of a factor of 3. It should be noted that the local field values can differ from the average field. For instance, if the brightness of the blobs is due to an increased magnetic field, at fixed \bar{s} , then the field in the blobs is a factor of 1.4 higher than the average field in the jet. On the other hand, the higher brightness can be explained by the projection effect (larger \bar{s}) and the Doppler boost ($\bar{s} \rightarrow \bar{s} \delta^{2+\Gamma}$ in eq. [1] if the bulk motion is taken into account).

Assuming equipartition, $w_{\text{rel}} = B^2/(8\pi) = 4 \times 10^{-10} B_{-4}^2 \text{ erg cm}^{-3}$, we can estimate the total energy of relativistic particles, $W_{\text{rel}} = 4 \times 10^{41} B_{-4}^2 V_{51} \text{ erg}$, where $V = 10^{51} V_{51} \text{ cm}^3$ is the volume of the jet. For plausible values of the magnetic field and the volume ($V_{51} \sim 0.2\text{--}1$, depending on the shape and orientation of the jet), we obtain $W_{\text{rel}} \sim 10^{40}\text{--}10^{42} \text{ erg}$. The energy injection rate and the energy flux can be estimated as $\dot{W} \sim 2W_{\text{rel}}/t_{\text{flow}} \approx 8 \times 10^{33} B_{-4}^2 (r_{\text{jet}}/1.5 \times 10^{16} \text{ cm})^2 (\beta/0.5) \text{ erg s}^{-1}$ and $F_W = \dot{W}/(\pi r_{\text{jet}}^2) \approx 10 B_{-4}^2 (\beta/0.5) \text{ erg cm}^{-2} \text{ s}^{-1}$, respectively, where r_{jet} is the jet radius, and βc is the flow speed. This injection rate is a small fraction of the spin-down energy loss rate of the Vela pulsar, $\dot{W} \sim 10^{-3} \dot{E}$. On the other hand, it greatly exceeds the observed X-ray luminosity of the jet, $L_{\text{x,jet}} \sim 10^{-3} \dot{W}$, which means that most of the injected energy is emitted outside the X-ray range or, more probably, carried out of the jet without substantial radiation losses.

One can also estimate the electron (positron) injection rate, $\dot{N}_{e,\text{jet}} = \dot{W} [2(1+k_i)m_e c^2 \bar{\gamma}]^{-1}$, where $\bar{\gamma} = [(p-1)(\gamma_M^{2-p} - \gamma_m^{2-p})] / [(2-p)[(\gamma_m^{1-p} - \gamma_M^{1-p})]]^{-1}$ is the average electron Lorentz factor for the power-law distribution. For the mean observed $\Gamma \simeq 1.3$, we have $\bar{\gamma} \approx 1.5 \gamma_M^{0.4} \gamma_m^{0.6}$ if $\gamma_m \ll \gamma_M$. Unfortunately, the minimum and maximum electron energies cannot be determined without multiwavelength observations of the jet, therefore we will scale $\bar{\gamma}$ to a possible (but arbitrary) value of 10^8 , which gives $\dot{N}_{e,\text{jet}} \approx 5 \times 10^{31} \bar{\gamma}_8^{-1} (1+k_i)^{-1} \text{ s}^{-1}$. This estimate corresponds to the mean electron number density $n_{e,\text{jet}} \sim w_{\text{mag}} (1+k_i)^{-1} (m_e c^2 \bar{\gamma})^{-1} \sim 5 \times 10^{-12} B_{-4}^2 (1+k_i)^{-1} \bar{\gamma}_8^{-1} \text{ cm}^{-3}$. The numerical estimates for $\dot{N}_{e,\text{jet}}$ and $n_{e,\text{jet}}$ strongly depend on the boundary energies of the electron power-law spectrum; in particular, the estimates become 3 orders of magnitude larger if γ_m is low enough ($\sim 10^3$) for the jet to be synchrotron-emitting in the radio band.

It is interesting to compare the estimate for $\dot{N}_{e,\text{jet}}$ with the pair production rate expected for the Vela pulsar: $\dot{N}_{e,\text{puls}} \sim n_{\text{GJ}} (4\pi^2 R^3/P) \kappa_{\text{pair}} = 4\pi^2 R^3 B_{\text{puls}} (c e P^2)^{-1} \kappa_{\text{pair}} \simeq 1.2 \times 10^{33} \kappa_{\text{pair}} \text{ s}^{-1}$, where n_{GJ} is the Goldreich-Julian density, $R \approx 10^6 \text{ cm}$ and $P = 0.089 \text{ s}$ are the neutron star radius and spin period, $B_{\text{puls}} = 3.4 \times 10^{12} \text{ G}$ is the pulsar magnetic field, and κ_{pair} is the pair multiplication coefficient (its plausible value

is $\kappa_{\text{pair}} \sim 10^3$ — see, e.g., Hibschan & Arons 2001). The ratio $\dot{N}_{e,\text{jet}}/\dot{N}_{e,\text{puls}} \sim 4 \times 10^{-5} (\kappa_{\text{pair}}/10^3) \bar{\gamma}_8^{-1} (1+k_i)^{-1}$ can be interpreted as the fraction of pairs escaping from the pulsar through the outer jet, assuming that no pairs are created in the jet itself. It is worth noting that the maximum Lorentz factor for the pairs created in the pulsar magnetosphere does not exceed a few $\times 10^7$, for both the polar cap models (Harding, Muslimov, & Zhang 2002, and references therein) and the outer gap models (e.g., Zhang & Cheng 1997). The maximum Lorentz factor in the outer jet, $\gamma_M > 5 \times 10^8$, is substantially higher, which means that the pairs, created by the pulsar, have been additionally accelerated beyond the pulsar magnetosphere.

If ions are pulled out of the neutron star surface layers, their outflow rate is constrained to the Goldreich-Julian value: $\dot{N}_{i,\text{puls}} \sim \dot{N}_{e,\text{puls}} (Z\kappa_{\text{pair}})^{-1} \simeq 1.2 \times 10^{33} Z^{-1} \text{ s}^{-1}$, while their characteristic energy may exceed that of electrons/positrons (Gallant & Arons 1994). Although the ions can be further accelerated to even higher energies, the maximum ion energy in the jet cannot exceed $\varepsilon_{i,M} \sim ZeBr_{\text{jet}} \sim 5 \times 10^{14} ZB_{-4}(r_{\text{jet}}/1.5 \times 10^{16} \text{ cm}) \text{ eV}$ [$\gamma_{i,M} \sim 5 \times 10^5 (Z/A)B_{-4}(r_{\text{jet}}/1.5 \times 10^{16} \text{ cm})$] because the Larmor radius of ions with higher energies is larger than the jet radius. Assuming that the ion-to-electron number density ratio in the jet does not exceed that in the magnetosphere outflow, we can constrain the ion-to-electron energy density ratio: $k_i = (n_{i,\text{jet}}\bar{\varepsilon}_{i,\text{jet}})/(n_{e,\text{jet}}\bar{\varepsilon}_{e,\text{jet}}) < (\dot{N}_{i,\text{puls}}/\dot{N}_{e,\text{puls}})(ZeBr_{\text{jet}}/m_e c^2 \bar{\gamma}) \sim 10^{-2} B_{-4} \bar{\gamma}_8^{-1} (10^3/\kappa_{\text{pair}})$, at $r_{\text{jet}} = 1.5 \times 10^{16} \text{ cm}$. This means that relativistic ions do not make a substantial contribution to the energetics of the outer jet.

Since the bulk velocities in the outer jet are only mildly relativistic, the bulk kinetic energy of relativistic particles is much lower than the energy of their random motion. However, we cannot rule out the possibility that some nonrelativistic electron-ion plasma from the ambient SNR medium is entrained into the jet via interaction with the jet’s magnetic field. To estimate an upper limit on the maximum density of the nonrelativistic component and maximum kinetic energy of the outer jet, it seems reasonable to assume that the *total* energy injection rate, including the kinetic energy, into the outer jet cannot exceed a fraction of $L_{\text{jet}}/L_{\text{pwn}} \approx 0.008$ of the total power, $\dot{E} \approx 7 \times 10^{36} \text{ erg s}^{-1}$, supplied by the pulsar, which implies $W_{\text{kin}} < 0.008 \dot{E} t_{\text{flow}} \sim 4 \times 10^{42} l_{\text{jet},18} (\beta/0.5)^{-1} \text{ erg}$. This condition requires densities of nonrelativistic particles (ions or electrons), $n_{\text{nonrel}} < 2 \times 10^{-4} (r_{\text{jet}}/1.5 \times 10^{16} \text{ cm})^{-2} (\beta/0.5)^3 \text{ cm}^{-3}$. Thermal X-ray radiation from such a low-density plasma is orders of magnitude fainter than the observed radiation from the outer jet. The corresponding upper limits on the pressure and energy density of the nonrelativistic components depend on the unknown mean energy of nonrelativistic particles; however, they do not exceed the pressure and energy density of relativistic particles and the magnetic field. Furthermore, the density of this plasma is much lower than the density of the ambient medium. On the other hand, the bulk pressure, $p_{\text{bulk}} \sim \rho v_{\text{bulk}}^2 < 7 \times 10^{-8} \text{ erg cm}^{-3}$, can be higher than the pressure in the ambient medium, $p_{\text{amb}} \sim 10^{-9} \text{ erg cm}^{-3}$.

3.3. End bend and outer PWN: Effect of SNR wind?

We see from Figures 3 and 4 that the outer jet is never straight, showing either gentle bends (e.g., panels 5–10) or a strongly curved structure (panels 1, 2, and 13). The varying

curvature of the outer jet can be explained by its interaction with the ambient medium (SNR plasma) and/or by a kink instability in the jet flow.

A strong argument for an external wind to cause jet’s bending is provided by the deep image of the PWN (Fig. 1) that allows one to see an extension of the outer jet beyond the apparent termination points (often associated with outermost blobs) observed in the individual images. It shows that the outer jet does *not* terminate abruptly, but it rather smoothly bends clockwise (towards west and then southwest) by at least 90° . Such bending suggests a persistent *northeast wind* in the ambient medium (approximately perpendicular to the direction of the pulsar’s proper motion). Such a wind could also explain the very asymmetric diffuse emission outside the bright PWN — the wind “blows off” relativistic electrons, produced in the bright PWN, towards the southwest. Moreover, it could explain, in the same way, the fact that the surface brightness is substantially higher at the southwest side of the outer jet compared with the northeast — some high-energy particles are leaking from the jet and blown away by the wind. Finally, an additional support for the wind comes from the radio image of the (outer) PWN (Lewis et al. 2002; Dodson et al. 2003b). This image shows two lobes, northeast and southwest of the X-ray bright PWN, with a much smaller northeast lobe confined by a brightened northeast boundary. The smaller size and the brightening can be explained by compression of the radio-emitting plasma by the external northeast wind. The bulk pressure of this wind can be crudely estimated as $P_{\text{wind}} \sim (d_{\text{jet}}/R_{\text{curv}})(\Theta/A_{\perp})$, where d_{jet} is the diameter of the jet, R_{curv} is the curvature radius of the bending, and Θ is the thrust (jet’s momentum flux) through the jet’s transverse area A_{\perp} (e.g., Leahy 1991). If the bulk kinetic pressure is much lower than the magnetic pressure within the jet, $\rho_{\text{jet}} v^2 \ll B^2/(8\pi) \sim 10^{-10} \text{ erg cm}^{-3}$, then the main contribution to the thrust comes from the longitudinal component of the magnetic stress tensor that, in turn, depends on the geometry of the magnetic field. For instance, we obtain $\Theta \sim A_{\perp} B^2/(24\pi)$ for a tangled magnetic field, which gives $P_{\text{wind}} \sim 3 \times 10^{-12} B_{-4}^2 \text{ erg cm}^{-3}$, for $R_{\text{curv}} \sim 3 \times 10^{17} \text{ cm}$. This bulk pressure is much lower than the typical thermal pressure in the Vela SNR. It corresponds to the wind velocity $v_{\text{wind}} \sim 10 n_{\text{wind}}^{-1/2} B_{-4} \text{ km s}^{-1}$, where n_{wind} is the ion (proton) number density in the wind. Attempts at separating the wind’s X-ray emission from the SNR background did not yield conclusive results. Assuming a low-density wind, $n_{\text{wind}} \sim 10^{-2} \text{ cm}^{-3}$, we obtain $v_{\text{wind}} \sim 100 B_{-4} \text{ km s}^{-1}$ — high but not improbable velocity. Such a velocity is comparable with the pulsar’s proper motion velocity, $\simeq 97 d_{300} \text{ km s}^{-1}$ (Caraveo et al. 2001), but the pulsar’s motion itself cannot initiate the observed bending because the pulsar moves in the direction of the unbent jet (at least in the sky projection). However, once the jet is substantially bent from its original direction by the putative SNR wind, the pulsar’s motion with respect to the SNR matter can bend it further, so that the jet can become directed backwards (towards southeast). A hint of such a bend is indeed seen in Figure 1. Moreover, the relativistic particles blown off the jet by the SNR wind are being picked up by the head wind (in the pulsar’s reference frame) and dragged in the direction opposite to the pulsar’s proper motion, feeding the diffuse nebula. Such a picture is supported by the spectral slope of the diffuse emission, $\Gamma \approx 1.5$, which is softer than the emission of the brighter outer jet ($\Gamma \approx 1.3$), but harder than the emission of the PWN shell ($\Gamma \approx 1.65$). Thus, we can con-

clude that the outermost observable part of outer jet is likely bent by the combined action of the SNR wind and the pulsar’s proper motion, and the outer jet finally bends backward and get diffused southwest of the pulsar.

3.4. Loop-like structures and blobs: Instabilities in pinched flow?

So far we have discussed only the bending of the jet’s “end”. Explaining more extreme bends in the brighter part of the outer jet (e.g., the hook-like or loop-like structures in panels 1, 2, 4, and 13) by the wind action is more problematic. Although we see that these bends are convex in the direction of the SNR wind suggested above, the relatively small size (and strong curvature) of these structures would require a strong nonuniformity and very high velocities of the wind. Even a stronger argument is the observed variability of the bent structures, associated with almost relativistic velocities. Therefore, we have to invoke another mechanism to explain these features, not related to external winds. A natural explanation is the kink instability of a magnetically confined, pinched flow. Estimates of the instability growth times and wavelengths depend on the model of such a flow, particularly the distribution of currents and topology of the magnetic field. The flow model is also tightly connected with the interpretation of the whole PWN, particularly the inner jets and arcs. Analysis of these models is beyond the scope of the present paper. Therefore, we only briefly mention that the (outer) jet can be modeled as a plasma beam carrying a charge current of $\sim 10^{32} e s^{-1}$ ($\sim \dot{N}_{\text{jet}}$ — see §3.2), self-confined by a predominantly toroidal magnetic field (Z pinch). A similar model for pulsar jets was suggested by Benford (1984), while collimation and confinement of AGN jets by magnetic field was reviewed by Begelman, Blandford & Rees (1984) and other authors. Growth times of MHD instabilities in such a flow are proportional to the Alfvén crossing time, $\tau_A \sim r_{\text{jet}}/v_A$ (e.g., Begelman 1998). Using the expression for the Alfvén velocity in the ultrarelativistic plasma, $v_A = cB[4\pi(w_{\text{rel}} + p_{\text{rel}}) + B^2]^{-1/2}$ (Akhiezer et al. 1975), we obtain $v_A = (3/5)^{1/2}c \simeq 0.77c$ at equipartition between the magnetic and particle energy densities, which gives $\tau_A \sim 10$ days. This time is comparable to the time scales of strong bendings ($\lesssim 30$ days), which can be associated with the kink instabilities, and time scales of blob brightening (about a week), which can be associated with the sausage (neck) instabilities.

4. SUMMARY AND CONCLUSIONS

The multiple *Chandra* observations of the Vela PWN have allowed us to investigate the dynamical outer jet and discover a dimmer outer counter-jet outside the bright PWN. Our main results can be summarized as follows.

1. The outer jet extends up to about 0.4–0.5 light years from the pulsar in the sky plane along the direction of the pulsar’s proper motion. Its shape and brightness are variable on time scales of days to weeks. The brightness is nonuniform along the jet, with brighter blobs moving away from the pulsar with apparent subrelativistic speeds. The variations observed suggest typical flow velocities of 0.3–0.7 of the speed of light.

2. The outer jet is, on average, a factor of 7 brighter than the outer counter-jet. If the outer jet and outer counter-jet are intrinsically similar but streaming in opposite directions, then the difference in brightness means that the outer jet is approaching at an angle of 30°–70° to the line-of sight while the outer counter-jet is receding. Such an orientation apparently

contradicts to the previously suggested models of the inner jets and the bright arcs.

3. The synchrotron interpretation of the hard ($\Gamma \approx 1.3$) power-law spectrum of the outer jet requires highly relativistic electrons or positrons, with energies of up to $\gtrsim 200$ TeV, and a typical magnetic field of about 100 μG . The outer jet’s spectrum is perhaps slightly softer than those of the inner jet and counter-jet, but it does not change appreciably along the outer jet. If the outer jet is a mildly relativistic outflow of an ultrarelativistic electron/positron plasma, the energy injection rate is $\sim 10^{34} \text{ erg s}^{-1} \sim 10^{-3} \dot{E} \sim 10^3 L_{\text{X, jet}}$.

4. Outside the bright PWN, there is an asymmetric, dim outer diffuse nebula that is substantially brighter southwest of the jet/counter-jet line. Its spectrum is softer than that of the outer jet, but it is harder than the spectrum of the brighter PWN shell. It is possible that the X-ray emitting particles in the dim nebula are supplied through the outer jet, whose end part turns southwest with respect to its average (northwest) direction in the sky plane. Such a turn can be caused by a northeast SNR wind with a speed of a few times 10 km s^{-1} , which also helps feed the dim nebula.

5. The width of the outer jet, $\sim 3 \times 10^{16}$ cm, remains approximately the same along the jet in different observations, including those which show strong bends. This suggests an efficient confinement mechanism, perhaps associated with magnetic fields generated by electric currents in the pinched jet. The current required, $\sim 10^{32} e s^{-1} \sim 10^{12}$ amp, is an order of magnitude lower than the Goldreich-Julian current in the pulsar magnetosphere. The bright blobs and strong bends could be caused by the sausage and kink instabilities, respectively, in such a pinched jet.

The excellent resolution of the *Chandra* telescope and high sensitivity of its detectors allowed us to obtain the spectacular pictures of the Vela PWN, including the faint outer jet, and, in particular, to prove the highly anisotropic and dynamical nature of the pulsar outflows. However, as has been often the case with new high-quality data, our results raise new questions and put under doubt the previous simplistic interpretations of PWNe in general and the Vela PWN in particular. The most unclear issue is the interpretation of the complicated morphology of the Vela PWN, particularly the relationship of the outer jet and outer counter-jet with their inner counterparts, the true orientation of the jets, and the actual topology of its arcs. We do not even know the actual three-dimensional orientations of the inner and outer jets and counter-jets, nor do we understand the cause of their different brightness. We can only guess about the nature of the bright blobs moving along the outer jet, the mechanism(s) of the jet confinement, and the origin of the jet bendings. At least some of these issues can be clarified by a series of deeper *Chandra* observations of the Vela PWN, taken with intervals of a few days, the now-established time scale of the PWN variations. In particular, such observations would allow one to search for the spectral changes along the outer jet and check if the spectra of the blobs are different from those of the rest of the jet. They could also help find blobs in the very dim outer counter-jet and measure their velocities, which would provide a clue to the geometry of the system.

The interpretation of the Vela PWN would be much easier if it were detected at other wavelengths, outside the X-ray range. So far, contrary to the much better studied Crab PWN, the Vela PWN has not been detected in the optical, mainly because of numerous relatively bright field stars and SNR fil-

aments in the pulsar vicinity (Mignani et al. 2003). To get rid of their light and detect the PWN or put a stringent upper limit on its brightness, the field must be observed in polarized light. It would also be very important to obtain a deep radio image the field around the Vela pulsar with arcsecond resolution (cf. Dodson et al. 2003b). Both the optical and radio observations would provide estimates on the lower frequencies of the synchrotron spectra (hence, lower energies of relativistic electrons), the critical parameters for evaluating the magnetic fields and the energetics of the observed PWN elements. Measuring polarizations of the optical and radio emission would be crucial to establish the directions of the magnetic field in

the PWN elements and understand their nature.

We thank Leisa Townsley and George Chartas for the advice on ACIS data reduction and Bing Zhang for useful discussions of pulsar physics. Support for this work was provided by the NASA through Chandra Awards GO1-2071X and GO2-3091X, issued by the Chandra X-Ray Observatory Center, which is operated by the Smithsonian Astrophysical Observatory for and on behalf of NASA under contract NAS8-39073. This work was also partially supported by NASA grant NAG5-10865.

REFERENCES

- [1]Aschenbach, B., & Brinkmann, W. 1975, *A&A*, 41, 147
- [2]Akhiezer, A. I., Akhiezer, I. A., Polovin, R. V., Sitenko, A. G., & Stepanov, K. N. 1975, *Plasma Electrodynamics*, (Oxford: Pergamon), p.112
- [3]Begelman, M. C. 1998, *ApJ*, 493, 291
- [4]Begelman, M. C., Blandford, R. D., Rees, M. J. 1984, *Rev. Mod. Phys.*, 56, 255
- [5]Benford, G. 1984, *ApJ*, 282, 154
- [6]Caraveo, P. A., De Luca, A., Mignani, R. P., & Bignami, G. F. 2001, *ApJ*, 561, 930
- [7]Dodson, R., Legge, D., Reynolds, J. E., & McCulloch, P. M. 2003a, *ApJ*, submitted (astro-ph/0302374)
- [8]Dodson, R., Lewis, D., McConnel, D., & Deshpande, A. A. 2003b, *MNRAS*, submitted (astro-ph/0302373)
- [9]Gaensler, B. M., Arons, J., Caspi, V. M., Pivovarov, M. J., Kawai, N., & Tamura, K. 2002, *ApJ*, 569, 878
- [10]Gallant, Y. A., & Arons, J. 1994, *ApJ*, 435, 230
- [11]Ginzburg, V. L., & Syrovatskii, S. I. 1965, *ARA&A*, 3, 297 [GS65]
- [12]Harding, A. K., Muslimov, A. G., & Zhang, B. 2002, *ApJ*, 576, 366
- [13]Harnden, F. R., Grant, P. D., Seward, F. D., & Kahn, S. M. 1985, *ApJ*, 299, 828
- [14]Helfand, D. J., Gotthelf, E. V., & Halpern, J. P. 2001, *ApJ*, 556, 380
- [15]Hester, J. J., Mori, K., Burrows, D., et al. 2002, *ApJ*, 577, L49
- [16]Hirschman, J., & Arons, J. 2001, *ApJ*, 560, 871
- [17]Kargaltsev, O., Pavlov, G. G., Sanwal, D., & Garmire, G. P. 2002, in *Neutron Stars in Supernova Remnants*, eds. P.Ö. Slane & B. M. Gaensler, ASP Conf. Ser., v.271 (San Francisco: ASP), 181
- [18]Leahy, J. P. 1991, in *Beams and Jets in Astrophysics*, ed. P. A. Hughes (Cambridge: Cambridge Univ. Press), 147
- [19]Lewis, D., Dodson, R., McConnel, D., & Deshpande, A. 2002, in *Neutron Stars in Supernova Remnants*, eds. P.Ö. Slane & B. M. Gaensler, ASP Conf. Ser., v.271 (San Francisco: ASP), 191
- [20]Markwardt, C. B., & Ögelman, H. 1998, *Mem. Soc. Astron. Italiana*, 69, 927
- [21]Mignani, R. P., De Luca, A., Kargaltsev, O., Pavlov, G. G., Zaggia, S., Caraveo, P. A., & Becker, W. 2003, *ApJ*, submitted
- [22]Mori, K., Hester, J. J., Burrows, D. N., Pavlov, G. G., & Tsunemi, H. 2002, in *Neutron Stars in Supernova Remnants*, ASP Conf. Ser., v. 271, eds. P. O. Slane & B. M. Gaensler (San Francisco: ASP), 157
- [23]Pacholczyk, A. G. 1970, *Radio Astrophysics* (San Francisco: Freeman)
- [24]Pavlov, G. G. 2000, *AAS HEAD Meeting 32*, #07.05
- [25]Pavlov, G. G., Sanwal, D., Garmire, G. P., Zavlin, V. E., Burwitz, V., & Dodson, R. G. 2000, *AAS Meeting 196*, #37.04
- [26]Pavlov, G. G., Kargaltsev, O. Y., Sanwal, D., & Garmire, G. P. 2001a, *ApJ*, 554, L189
- [27]Pavlov, G. G., Zavlin, V. E., Sanwal, D., Burwitz, V., & Garmire, G. P. 2001b, *ApJ*, 552, L129
- [28]Plucinsky, P. P., et al. 2002, in *Astronomical Telescopes and Instrumentation 2002*, eds. J. E. Tr mper & H. D. Tananbaum, SPIE Conf. Proc., in press (astro-ph/0209161)
- [29]Radhakrishnan, V., & Deshpande, A. 2000, *A&A*, 379, 551
- [30]Townsley, L. K., Broos, P. S., Garmire, G. P., & Nousek, J. A. 2000, *ApJ*, 534, L139
- [31]Zhang, L., & Cheng, K. S. 1997, *ApJ*, 487, 370